

Water–Silica Force Field for Simulating Nanodevices

Eduardo R. Cruz-Chu,^{†,‡} Aleksei Aksimentiev,^{†,§} and Klaus Schulten^{*,†,‡,§}

Beckman Institute for Advanced Science and Technology, Center for Biophysics and Computational Biology, and Department of Physics, University of Illinois at Urbana-Champaign, Urbana, Illinois 61801

Received: June 22, 2006; In Final Form: August 28, 2006

Amorphous silica is an inorganic material that is central for many nanotechnology applications, such as nanoelectronics, microfluidics, and nanopore sensors. To use molecular dynamics (MD) simulations to study the behavior of biomolecules interacting with silica, we developed a force field for amorphous silica surfaces based on their macroscopic wetting properties that is compatible with the CHARMM force field and TIP3P water model. The contact angle of a water droplet on a silica surface served as a criterion to tune the intermolecular interactions. The resulting force field was used to study the permeation of water through silica nanopores, illustrating the influence of the surface topography and the intermolecular parameters on permeation kinetics. We find that minute modeling of the amorphous surface is critical for MD studies, since the particular arrangement of surface atoms controls sensitively electrostatic interactions between silica and water.

1. Introduction

Amorphous silica (SiO_2) is an inorganic material commonly used in semiconductor circuits to isolate different conducting regions. Due to its mechanical properties, high dielectric strength, and selectivity for chemical modification, amorphous silica has become a key material in microelectronics¹ and chromatography.² In recent years, the convergence of molecular biology and nanotechnology has opened up opportunities for many applications that involve macromolecules and silica, such as nanoelectronics,³ self-assembly of nanostructures,⁴ microfluidics,⁵ and DNA microarray technology.⁶ An atomic level understanding of the interactions between biomolecules and silica is now central for further development of nanobiotechnology applications. A combination of spectroscopic and molecular biology tools allows one to infer such interactions in principle,^{7,8} but no experimental technique is yet sensitive enough to resolve atomic-resolution dynamics at the amorphous interface. In addition, solvent conditions such as pH and ionic strength affect the interplay of biomolecules with silica.^{7,9–11} Molecular dynamics (MD) simulations can provide detailed interfacial properties involving silica and physiological solutions. Such simulations have been used previously to study systems composed of biomolecules and inorganic crystals,¹² and they can be tailored to study noncrystalline inorganic systems.

One of the most promising technologies that can benefit from molecular dynamics studies are solid-state or synthetic nanopore sensors. Recent advances in silica nanotechnology have been exploited to manufacture pores in thin synthetic membranes with subnanometer precision.^{13,14} Immersed in an electrolytic solution and under the influence of an electric field, nanopores can be deployed to filter and monitor translocation of DNA and other charged macromolecules. It has been suggested that synthetic nanopores could be used to sequence DNA with single base

precision,^{15–17} leading eventually to a low cost DNA sequencing technology that would have an enormous impact on life sciences and personal medicine.^{18,19} In the development of synthetic nanopores, MD simulations have been already deployed to describe the translocation of DNA molecules through Si_3N_4 nanopores, bringing about accurate quantitative predictions in close agreement with experimental measurements.^{20–22} Furthermore, MD is being used to aid the design of synthetic nanopores in MOS capacitor membranes composed of silica, silicon, and poly-silicon layers.^{23,24} Such nanopores are expected to increase the sensitivity of the measurements to single-base resolution.

Until recently, atomic-scale simulations of inorganic and biomolecular materials, such as silica and DNA, have mostly evolved independently from each other, and the consolidation of expertise from both areas demands now a great effort. Key in modeling these hybrid systems are the interactions among the solid surface, biopolymers, and water.^{25,26} These interactions are defined through the potential energy function of the system, the force field, that returns, in simulations, the interacting forces between atoms as a function of their atomic coordinates.

The atomic-scale topography of silica has an effect on the ionic environment and desolvation properties of biopolymers; thus, a careful description of the solid–liquid interface is needed.^{27,28} Amorphous silica has two types of exposed functional groups at the surface: silanols ($-\text{SiOH}$) and siloxanes ($-\text{SiO}-$). Qualitatively, one can assign a hydrophilic characteristic to a silanol group, since its hydroxyl group can hydrogen-bond with water and other molecules; a siloxane group with its oxygen partially buried can be considered hydrophobic. Silanol and siloxane groups shape the solvent accessible regions of the surface and define interactions of silica with other molecules. As the surface concentration of silanols decreases, the area covered by siloxanes increases and the silica surface becomes more hydrophobic. There is a clear relationship between the concentration of hydrophilic/hydrophobic groups and the wetting properties of the surface; the more hydrophobic the surface, the

* Corresponding author. E-mail: kschulte@ks.uiuc.edu.

[†] Beckman Institute for Advanced Science and Technology.

[‡] Center for Biophysics and Computational Biology.

[§] Department of Physics.

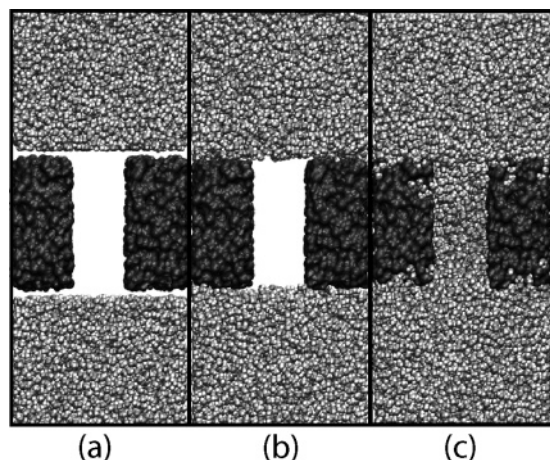


Figure 1. Force field parameters determine the wetting properties of silica nanopores. (a) Initial setup of the system: A nanopore of 20 Å diameter drilled through an amorphous silica box of dimensions 57 Å × 57 Å × 44 Å (dark gray) is shown surrounded by two water boxes, each with 6062 water molecules (light gray). Snapshots after a 1 ns MD simulation using the TIP3P water model and silica force fields taken from (b) Hill et al.³⁵ and (c) Tsuneyuki et al.³⁴ (van der Waals interactions were approximated using Lennard-Jones 6–12 potential). The Hill et al. force field (b) produces a hydrophobic pore, and water does not wet the pore. Conversely, the Tsuneyuki et al. force field (c) produces a hydrophilic pore, allowing water to permeate.

more water avoids contact, forming isolated droplets instead of a continuous thin layer. Likewise, small organic molecules that are capable of hydrogen bonding are easily adsorbed by a hydroxylated silica surface.^{29,30}

Due to the amorphous nature of silica, not all silanols are chemically equivalent. In fact, silanols can be classified as single isolated silanols, which have no other silanol next to them, and vicinal silanols, which can hydrogen-bond to neighboring silanols. An additional category is formed by geminal silanols that have two hydroxyl groups joined to the same silicon atom. The pK_a values for isolated and vicinal silanols have been estimated as 4.9 and 8.5,³¹ respectively; however, their relative concentrations depend on the thermal history of the sample. As a result, amorphous silica has a heterogeneous surface with an overall negative charge that increases with pH and ionic concentration of the solution.^{32,33}

Since interactions with biomolecules in all present biotechnical applications of silica occur in an aqueous environment, an empirical force field for silica should be able to reproduce its surface wetting properties. However, existing force fields for silica^{34–37} were parametrized to describe primarily its bulk physical properties correctly and then refined to reproduce the geometry of the silica surface,³⁸ but the force fields were not validated to describe interactions with biopolymers in aqueous solution. Furthermore, the functional form for the potential energy in available force fields is not compatible with the water models used in biomolecular simulations, i.e., TIP3P³⁹ or SPC.⁴⁰

Because of the lack of a suitable force field, silica potentials have been used beyond their validated conditions to study the interactions of water,^{41–43} small organic molecules,⁴⁴ and ions⁴⁵ with silica nanopores. Although those studies have captured different experimental features of the confined nanopore environment, combining different silica force fields with the same water model can produce completely different outcomes as illustrated rather dramatically in Figure 1.

Another important aspect that needs to be taken into account is the heterogeneity of amorphous surfaces. Garofalini et al. have studied the reconstruction of silica surfaces^{46–50} and several

MD studies^{51,52} have shown that the particular arrangement of the exposed silica atoms is crucial for understanding the surface properties. A recently published force field,⁵³ describing the interactions between regular crystalline quartz and water using ab initio calculations followed a procedure that has been extensively used to parametrize DNA and proteins.^{54,55} However, most technical applications deal with amorphous silica in which properties such as adsorption, pK_a , charge density, and surface topography diverge from those of an ordered crystal of quartz. Moreover, crystalline quartz in solution develops a layer of amorphous silica.²⁷

In this paper we tackle the force field parametrization problem for silica using an approach proposed by Werder et al.²⁶ This approach selects force field parameters such that macroscopic properties, namely the hydrophobicity of the surface, are reproduced well. For this purpose, the contact angle of a water droplet on a silica surface, referred to as the water contact angle (WCA), is used to tune the intermolecular silica–water interactions. The resulting force field parameters can then also be used to describe the interactions of silica with biological macromolecules. Future work will explore how accurately such descriptions are. Below, we describe how to build atomic-scale models of silica surfaces and silica pores using computational procedures that mimic experimental annealing and reproduce structural features of amorphous silica with great accuracy. We then select force field parameters to match the wetting characteristics of silica as captured through the WCA. Finally, we investigate wetting of silica nanopores.

2. Methods

In this section, the force fields, assembled system, simulation conditions, and simulation analysis tools are presented. To obtain amorphous silica structures, we employed the program Cerius² v. 4.9⁵⁶ from Accelrys; for silica–water dynamics we used the molecular dynamics program NAMD 2.5,⁵⁷ the simulation outcomes were analyzed through our own routines programmed in MatLab v. 6⁵⁸ and in VMD.⁵⁹

2.1. Force Fields. The GLASSFF_2.01 and GLASSFF_1.01 force fields provided in Cerius² were deployed to produce amorphous silica surfaces and pores. The GLASSFF_2.01 force field includes two contributions, a two-body and a three-body nonbonded potential:

$$U_{\text{total}} = \sum_{i < j} U_2(i, j) + \sum_{i < j < k} U_3(i, j, k) \quad (1)$$

$$U_2(i, j) = A_{ij} \exp\left[\frac{-r_{ij}}{\rho_{ij}}\right] + \frac{Z_i Z_j e^2}{r_{ij}} \operatorname{erfc}\left(\frac{r_{ij}}{\beta_{ij}}\right) \quad (2)$$

$$U_3(i, j, k) = h(r_{ij}, r_{ik}, \phi_{jik}) + h(r_{jk}, r_{ji}, \phi_{kji}) + h(r_{ki}, r_{kj}, \phi_{ikj}) \quad (3)$$

The two-body potential $U_2(i, j)$ is composed of a repulsive van der Waals (vdW) term and an electrostatic Coulombic term screened with a complementary error function (erfc) that reduces the interaction between the ionic charges Z_i and Z_j . e is the electron charge; r_{ij} is the distance between atoms i and j ; A_{ij} , β_{ij} , and ρ_{ij} are adjustable parameters. The three-body potential $U_3(i, j, k)$ introduces a directional contribution to induce a tetrahedral arrangement of the silica glass.

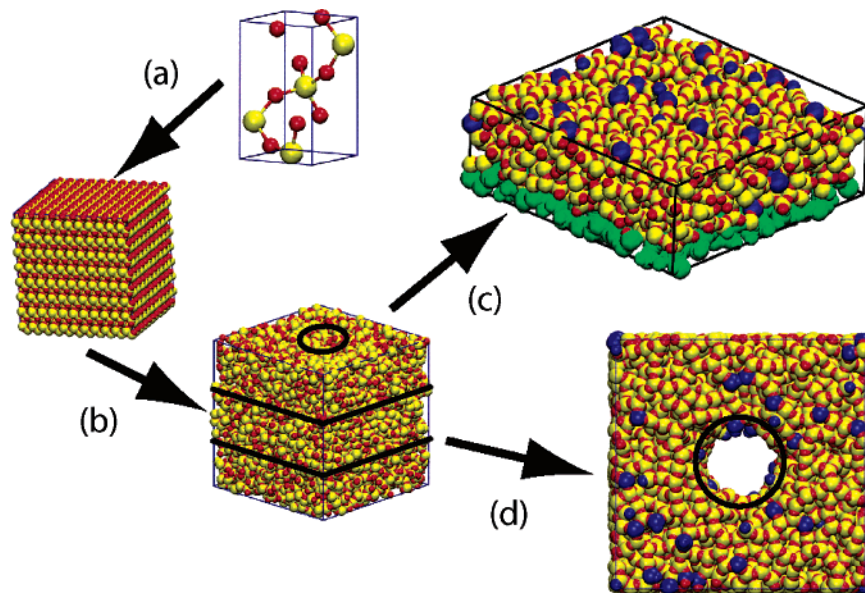


Figure 2. Building silica surfaces and silica pores. (a) A cristoballite unit cell was replicated, filling a cube of $57 \text{ \AA} \times 57 \text{ \AA} \times 57 \text{ \AA}$. (b) To obtain amorphous bulk, the crystalline silica was annealed, increasing the temperature to 8000 K and then lowering it back to 300 K. The cube of bulk material was sliced and annealed to create silica surfaces and silica pores. (c) A 20-Å-thick slab of amorphous silica (black rectangle) is annealed further to produce amorphous silica surfaces. Atoms located 4 Å from the bottom of the slab were fixed (shown in green). (d) After drilling a silica pore of 10 Å radius (black circle), the structure was annealed to produce silica pores. By varying the annealing conditions (Table 1), different concentrations of dangling atoms at the surface (shown in blue) were obtained.

Here, we define $h(r_{ij}, r_{ik}, \phi_{jik})$ through

$$h(r_{ij}, r_{ik}, \phi_{jik}) = \begin{cases} \lambda_1 \exp \left[\frac{\gamma_i}{r_{ij} - r_i^c} + \frac{\gamma_i}{r_{ik} - r_i^c} \right] (\cos \phi_{jik} - \cos \phi_{jik}^c)^2, & r_{ij} < r_i^c \text{ and } r_{ik} < r_i^c \\ 0, & r_{ij} \geq r_i^c \text{ or } r_{ik} \geq r_i^c \end{cases} \quad (4)$$

This term produces an energy bias toward the angle ϕ_{jik}^c ; the angle is determined by the atoms j and k , with a vertex at i , only when the atoms j and k are within the radial distance r_i^c . λ_i and γ_i are adjustable parameters.^{47,60} The force field GLASSFF_1.01 is an earlier version of GLASSFF_2.01 and includes only the two-body potential (eq 2). GLASSFF_1.01 has been used below to obtain a hydrophobic silica surface (see subsection 3.1).

To parametrize a force field that can account for silica–water interactions and subsequently also for silica–biopolymer interactions, we employed a potential energy function compatible with the CHARMM force field. We began with previously existing parameters for silicon and oxygen atoms and refined them to reproduce the interactions of silica with water. The functional form used is

$$U_{\text{total}} = U_{\text{bond}} + U_{\text{angle}} + U_{\text{vdW}} + U_{\text{Coulomb}} \quad (5)$$

The first two terms on the right-hand side of eq 5 are harmonic potentials used to describe bond stretching and bending:

$$U_{\text{bond}} = \sum_{\text{bonds } i} k_i^{\text{bond}} (r_i - r_{0i})^2 \quad (6)$$

$$U_{\text{angle}} = \sum_{\text{angles } i} k_i^{\text{angle}} (\theta_i - \theta_{0i})^2 \quad (7)$$

Here the sums run over all bonds and bond angles; the parameters k_i^{bond} , k_i^{angle} , r_{0i} , and θ_{0i} describe the equilibrium

values of the degrees of freedom. The bonded interactions of silica were taken from Hill et al.³⁵ but adjusted to fit eqs 6 and 7.

The last two terms in eq 5 describe the vdW and electrostatic nonbonded interactions that are the main focus of this work:

$$U_{\text{vdW}} = \sum_i \sum_{j>i} \epsilon_{ij} \left[\left(\frac{r_{ij}^{\text{min}}}{r_{ij}} \right)^{12} - 2 \left(\frac{r_{ij}^{\text{min}}}{r_{ij}} \right)^6 \right] \quad (8)$$

$$U_{\text{Coulomb}} = \sum_i \sum_{j>i} \frac{q_i q_j}{4\pi\epsilon_0 r_{ij}} \quad (9)$$

The vdW interactions are represented through a Lennard–Jones 6–12 potential, with two adjustable parameters: r_{ij}^{min} , the distance at which the energy between atoms i and j is minimal, and ϵ_{ij} , the well depth. In the case of the oxygen atom, vdW parameters were taken from the CHARMM force field, assigning 3.5 \AA to $r_{\text{O}}^{\text{min}}$ and 0.15 kcal/mol to ϵ_{O} . For silicon, $r_{\text{Si}}^{\text{min}}$ was set to 4.295 \AA , corresponding to the silicon atomic radius.^{61,62} The value of ϵ_{Si} was estimated from the wettability of silica (subsection 3.4). The electrostatic interactions were calculated using eq 9, q_i and q_j being the partial atomic charges of atoms i and j , and ϵ_0 being the vacuum permittivity. The charges corresponding to silicon (q_{Si}) and oxygen (q_{O}) were tuned to reproduce the silica wettability (subsection 3.4). We employed the TIP3P model of water, since the CHARMM force field works best with this choice of model and its functional form conforms to eq 5.

2.2. Building Silica Structures. The schematic procedure for building silica structures is shown in Figure 2. First, we build a model of bulk amorphous silica. As described below, pieces of the bulk material were sliced to create slabs of amorphous silica and to introduce pores. To maintain electro-neutrality of the systems, a few atoms were removed from the surfaces, enforcing a ratio of two oxygen atoms per one silicon atom. Subsequently, the sliced systems were annealed. After

TABLE 1: Summary of Annealing Simulations for Silica Surfaces (SURF_nn) and Silica Pores (PORE_nn)^a

	annealing cycle				results			
	initial temp (K)	initial time (ps)	cooling step (K/ps)	total time (ps)	[DO] (nm ⁻²)	[DSi] (nm ⁻²)	[DA] (nm ⁻²)	accessible surface area (nm ²)
silica slabs								
SURF_2b	5000	20	100/5	255	0.031	0.062	0.092	39.118
SURF_3b1	5000	20	100/5	255	0.369	0.462	0.831	42.731
SURF_3b2	1000	10	700/10	20	0.985	1.108	2.093	42.384
SURF_3b3	300	50		50	1.016	1.200	2.216	42.884
SURF_3b4	1000	10	100/2	24	1.108	1.631	2.739	42.838
SURF_3b5	300	10		10	1.170	1.662	2.832	43.438
SURF_Raw					3.232	2.585	5.817	50.411
silica pores								
PORE_2b	5000	10	100/2	104	0.027	0.000	0.027	42.952
PORE_3b1	5000	10	100/2	104	0.371	0.239	0.610	48.345
PORE_3b2	1000	10	100/2	24	0.981	0.637	1.618	47.550
PORE_Min					1.167	0.875	2.042	49.421
PORE_Raw					2.653	1.592	4.244	45.102

^a Simulations were performed assuming an *NVT* ensemble. The final annealing temperature was 300 K in all cases. Concentrations of dangling atoms [DA], dangling oxygens [DO], and dangling silicons [DSi] were calculated using a constant area of 32.5 nm² for surfaces and 35.8 nm² for pores. The solvent accessible surface area was calculated using the SASA command provided in VMD,⁵⁹ with an expanded atom radius of 2 Å. Simulations to obtain SURF_2b and PORE_2b were performed with the GLASSFF_1.01 force field; all other simulations were performed using the GLASSFF_2.01 force field. For slabs SURF_3b2 and SURF_3b3, atoms 4 Å from the bottom were fixed; for slabs SURF_3b4 and SURF_3b5, atoms 15 Å from the bottom were fixed. SURF_Raw and PORE_Raw were neither minimized nor annealed, yielding the surfaces with the highest concentrations of DAs. PORE_Min was minimized, but not annealed.

annealing, the silica atoms in the resulting structures were classified according to their connectivity. Two atoms were considered covalently bonded if they had a separation distance of 2 Å or less. Oxygens with two or more bonds and silicons with four or more bonds were classified as a nondangling atom (non-DA) type. Oxygens with less than two bonds and silicons with less than four bonds were classified as a dangling oxygen (DO) type and dangling silicon (DSi) type, respectively, or just as a dangling atom (DA) type. These classifications were used extensively in the analysis of material properties.

To generate silica slabs and silica pores we used the *Minimizer* and *Dynamics* modules of Cerius² 4.9.⁵⁶ Simulations were performed using an integration time step of 1 fs and assuming periodic boundary conditions as well as an *NVT* ensemble (unless stated otherwise). Temperature and pressure were controlled using a Nosé–Hoover thermostat. To permit full electrostatic calculations via PME summation, the systems were made periodic in all directions with the elementary cell extended in the Z-direction to accommodate empty space above (and by virtue of periodicity also below) the silica surfaces.⁶³ All silica systems were minimized using the “Smart Minimizer” procedure provided with the *Minimizer* module of Cerius² 4.9, which employs a Steepest Descent minimization method at the beginning of the calculation, followed by a Quasi-Newton and a Truncated Newton minimization method at the end of the run, until convergence criteria are satisfied.

To create bulk amorphous silica, we replicated a low-crystoballite unit cell 11 × 11 × 8 times, filling a 57 Å × 57 Å × 57 Å box and yielding a system of 11 616 atoms. This step was followed by the annealing cycle 2-VIII proposed by Huff et al.⁶⁴ that employed the silica force field GLASSFF_2.01. The final amorphous system had a periodicity of 57.3 Å × 57.3 Å × 58.2 Å. The connectivity was calculated for each atom using a cutoff radius of 2 Å. 99.51% of the oxygens were bicoordinated, and 97.22% silicons were four-coordinated, which is in good agreement with Huff et al.’s results.

To furnish different silica surfaces, a slab of 20 Å height comprising 3981 atoms was cut from the 3D periodic bulk silica and annealed using the GLASSFF_2.01 force field and different

heating and cooling rates. The GLASSFF_1.01 was employed to produce a surface with very few DAs. For all annealing cycles, atoms 4 Å from the bottom in the Z-direction were fixed⁴⁷ and the periodicity of the original bulk cell was kept constant, which created a 30 Å slab of vacuum above the silica surface. Table 1 defines the seven surfaces produced and lists the respective concentration of DAs, DOs, and DSis. We will refer to these surfaces as annealed surfaces.

Once the annealed surfaces were obtained, they were replicated 2 × 2 times in the X- and Y-directions and used as templates to build silica slabs with four extra surface modifications, which we will refer to as surfaces of type I, II, III, and IV. All silica surfaces are illustrated in Figure 3. Figure 3a shows the annealed surface, with DOs and DSis present at the surface. Figure 3b shows the surface of type I; in this case all DSis were capped with oxygens producing a surface with DOs but no DSis. Figure 3c shows the surface of type II, DAs were converted to silanol groups by adding hydrogens to DOs and hydroxyl groups to DSis.

For annealed surfaces and surfaces of type I and II, the number of DAs, and, consequently, the number of surface modifications, is determined by the annealing cycles. To have control of the silanol concentration, silanols were also generated by randomly breaking siloxane bonds (–SiO–) starting with a surface with very few DAs (cf. surface Surf_2b in Table 1). Figure 3d shows the surface of type III; in this case each broken –SiO– bond that produces a pair of DAs was converted to silanol groups by adding a hydrogen to the DO and a hydroxyl group to the DSi. Figure 3e shows the surface of type IV, created in the same way as the surface of type III, but with one silanol of each pair of vicinal groups being deprotonated; a harmonic bond between hydrogen and oxygen was enforced to mimic a hydrogen bond (green dashed line, see below).

To produce silica pores, atoms were removed from the center of the SiO₂ amorphous cube, creating a cylindrically shaped channel of 10 Å radius with the symmetry axis parallel to the Z-axis. This resulted in a system of typically 10 500 atoms. Two different annealing cycles were performed using the GLASSFF_2.01 force field. A third simulation was performed using

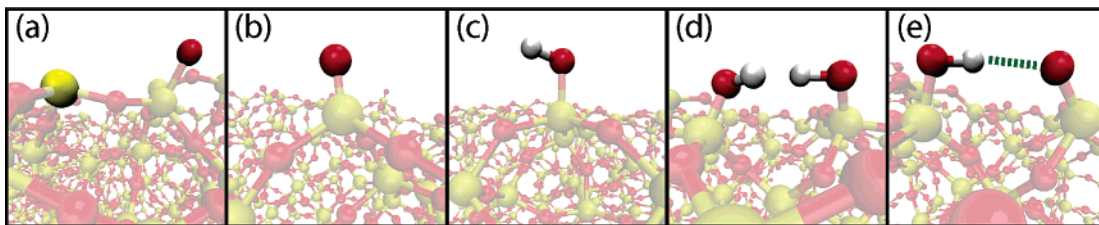


Figure 3. Five models for silica surfaces. All surfaces are composed of nondangling atoms along with five different modifications: (a) Annealed surface with dangling silicon and oxygen atoms (opaque yellow and red atoms, respectively). (b) Surface of type I with only dangling oxygens (opaque red atom). (c) Surface of type II with silanols. (d) Surface of type III with vicinal silanols. (e) Surface type IV with deprotonated vicinal silanols, a hydrogen bond between each pair of silanols being enforced (green dashed line; see subsection 2.3 and Figure 4).

the GLASSFF_1.01 force field to prepare a pore with very few DAs. For all silica pore annealings, neither fixed atoms nor harmonic restraint forces were applied and the periodicity along the Z-axis was increased to 116.3 Å in order to provide 59 Å of empty space above the surface. Table 1 summarizes the pores obtained and their respective concentration of DOs, DSis, and DAs at the surface. We will refer to the systems below as annealed pores.

2.3. Silica–Water Systems. To simulate silica–water systems we employed the molecular dynamics program NAMD 2.5.⁵⁷ Cylindrical and rectangular volumes of water were generated from a pre-equilibrated water box using the solvate plugin of VMD.⁵⁹ The silica structures were maintained rigid by fixing or restraining atomic coordinates to their original positions (see below), while water molecules were allowed to move freely. All simulations involving silica–water systems were carried out using a CHARMM compatible form of the potential energy function (eq 5). Simulations were performed with an integration time step of 1 fs and periodic boundary conditions at 300 K. vdW interactions were calculated with a cutoff of 12 Å (switching function starting at 10 Å), and the long-range electrostatic forces were calculated using the PME summation method. A multiple time stepping algorithm^{65,66} was employed to compute interactions involving covalent bonds every time step, short-range nonbonded interactions every two time steps, and long-range electrostatic forces every four time steps. A Langevin thermostat was used to maintain a constant temperature in the NVT ensemble simulations. Simulations in the NpT ensemble were performed using a hybrid Nosé–Hoover Langevin piston.⁶⁷ The simulation conditions adopted and the underlying algorithms have been summarized recently in a review describing the program NAMD.⁵⁷

To simulate the WCA of silica, a water disk with a radius and height of 30 Å composed of 1981 molecules was placed on top of each surface. All systems were minimized for 1000 steps of 1 fs using the conjugate gradient method and then equilibrated for 2 ns in the NVT ensemble. The elementary cell extension of the systems was 114.6 Å × 114.6 Å × 158.1 Å. To keep the amorphous slab rigid, the silica atoms were either fixed or restrained to their original position by applying a harmonic force with a force constant of 1 kcal/mol/Å². Tables 2 and 3 summarize the parameters used for the various silica slabs and specify which atoms were either fixed or restrained.

In the case of surfaces of type III and IV, oxygen atoms directly connected to silanols were allowed to move while the rest of the silica was restrained. Such relaxation was required for the following reasons: the silanols were generated by breaking bonds and adding hydroxyl groups; however, the latter gave rise to strong repulsive forces that relaxed only when the first layer of atoms connected to the silanol groups were free to rearrange.

TABLE 2: Summary of Fixed Atoms and Intermolecular Parameters Used in Simulations of Silica Slabs without Explicit Silanol Groups^a

surface	fixed	parameters for surface modifications
annealed	all atoms	q_{Si} : 0.1, 0.3, 0.5, 0.7, 0.9, 1.1 e ϵ_{Si} : 0.06, 0.1, 0.2, 0.3, 0.4 kcal/mol $r_{\text{Si}}^{\text{min}}$: 4.295 Å q_{O} : $-0.5 \times q_{\text{Si}}$ ϵ_{O} : 0.15 kcal/mol $r_{\text{O}}^{\text{min}}$: 3.5 Å
type I	all atoms except DO	q_{DO} : -0.0, -0.1, -0.3, -0.5, -0.7, -0.9, -1.1 e ϵ_{DO} : 0.3 kcal/mol $r_{\text{DO}}^{\text{min}}$: 3.5 Å

^a For annealed surfaces, bulk and surface atoms have the same parameters. For surfaces of type I, parameters for bulk atoms were fixed to the values q_{Si} , 0.9 |e|; ϵ_{Si} , 0.3 kcal/mol; $r_{\text{Si}}^{\text{min}}$, 4.295 Å; q_{O} , -0.45 |e|; ϵ_{O} , 0.15 kcal/mol; $r_{\text{O}}^{\text{min}}$, 3.5 Å, while the charge of DO, q_{DO} , was changed as shown in the table.

To evaluate the partial atomic charges of silanol groups, the respective charges were divided according to the scheme (see Figure 4):

$$q_{\text{total}} = q_{\text{vicinal}} + q_{\text{neigh-O}} \quad (10)$$

where q_{total} is the total charge of each pair of silanol groups and its neighboring oxygens, $q_{\text{neigh-O}}$ is the half of the charge corresponding to six oxygens, and q_{vicinal} is the charge of each pair of vicinal silanols. The initial charges for the silanol hydroxyl group were taken from the serine hydroxyl group of the charmm force field.⁵⁵ Subsequently, q_{total} was changed from 0 to -1 |e| in decrements of 0.25 |e| according to eq 10, and the resulting charge was evenly distributed over the silanol atoms contributing to q_{vicinal} .

To perform MD simulations with full electrostatics under periodic boundary conditions, the total charge of the system has to be zero. However, when adding modifications to annealed surfaces, different proportions of atoms are added, resulting in a total charge not necessarily equal to zero. Electroneutrality was recovered by scaling down the charge for all silica atoms below the modifications.²¹ For all charges modified, the adjustment was less than 0.5% of the initial charge value.

To study the permeation of silica nanopores, two identical cubic water boxes of 185.2 nm³ volume, each containing 6062 water molecules, were placed above and below the annealed pores. The resulting systems were minimized for 400 steps of 1 fs using the conjugate gradient method and then equilibrated in a 1 ns MD simulation. In the case of NVT ensemble simulations, the silica pores were fixed geometrically, whereas, in the case of NpT ensemble simulations, the silica atoms

TABLE 3: Summary of Fixed Atoms, Harmonic Restraints, and Intermolecular Parameters Used in Simulations of Silica Slabs with Explicit Silanol Groups^a

surface	fixed	harmonic restraints	parameters for surface modifications
type II	all atoms except hydroxyl group		OH from CHARMM OH from TIP3P
type III		all atoms except SiOH and oxygen atoms directly connected to SiOH	OH from CHARMM, but q_{total} varied according to eq 10 from 0 to $-1 e $ in decrements of $0.25 e $ (cf. subsection 2.3)
type IV		all atoms except SiOH and oxygen atoms directly connected to SiOH	OH from CHARMM, but q_{total} varied according to eq 10 from 0 to $-1 e $ in decrements of $0.25 e $ (cf. subsection 2.3)

^a Parameters for bulk atoms were fixed to the values q_{Si} , $0.9 |e|$; ϵ_{Si} , 0.3 kcal/mol ; $r_{\text{Si}}^{\text{min}}$, 4.295 \AA ; q_{O} , $-0.45 |e|$; ϵ_{O} , 0.15 kcal/mol ; $r_{\text{O}}^{\text{min}}$, 3.5 \AA . Bond stretching and bending terms for OH were taken from either CHARMM or TIP3P. In the case of OH from CHARMM, the hydroxyl group was taken from the serine group.

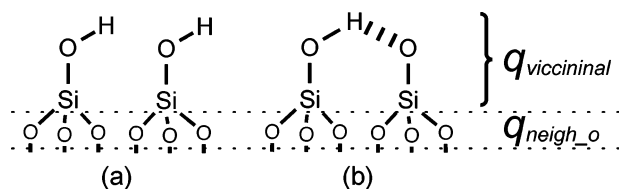


Figure 4. Charge distribution for silanol groups on surfaces of type III and IV. (a) In the surface of type III, q_{vicinal} gets contributions from six atoms. (b) In the surface of type IV, q_{vicinal} is composed of five atoms, a hydrogen bond is enforced between vicinal silanols (dashed line) with a spring constant of $5.5 \text{ kcal/mol/\AA}^2$ and an equilibrium distance of 3.5 \AA . In both cases, (a) and (b), q_{neigh_o} is the half of the charge of the six oxygens and the total charge q_{total} was modified from 0 to $-1.0 |e|$ according to eq 10. The resulting charge was evenly distributed over the silanol atoms in q_{vicinal} .

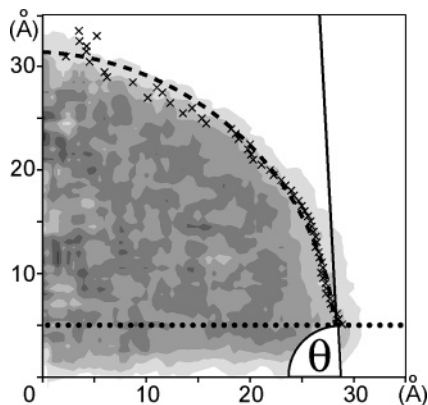


Figure 5. Calculation of the water contact angle (WCA). The contour plot shows the radial density profile of a water droplet (gray tones). First, the surface of the water droplet (crosses) is calculated from the density profile using eq 11. Then, the resulting surface is fitted to a circular segment (dashed line). The WCA (θ) is the angle between the tangent of the fitted circle and the silica surface. The water below 5 \AA from the silica surface (dotted line) is excluded from the calculations.

were restrained by applying a harmonic force with a spring constant of 5 kcal/mol/\AA^2 . For these simulations we used the force field parameters determined from the simulations of a water droplet on annealed silica slabs (see subsection 3.4 and Table 4).

2.4. Analysis. The calculation of the water contact angle⁶⁸ is schematically presented in Figure 5. The density profile was computed using horizontal layers of 3 \AA height. Each layer was displaced by 0.5 \AA in the Z-direction, starting from the base and ending at the top of the droplet. Within each layer, the radial density was calculated using circular bins of 3 \AA thickness that

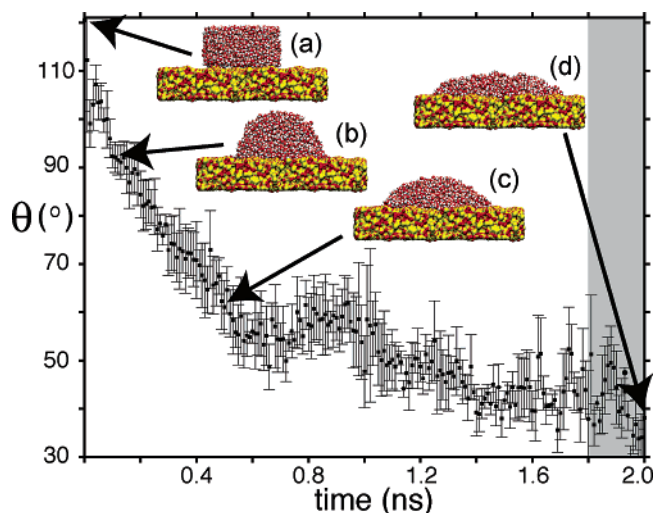


Figure 6. Variation of the WCA (θ) during an equilibration of a water droplet on an annealed surface (cf. Figure 3a). The error bars reflect the deviation of the droplet's contact line from a circle. (a) Initial configuration with a water disk of 30 \AA height and 60 \AA diameter placed on top of an annealed silica slab of $114 \text{ \AA} \times 114 \text{ \AA} \times 20 \text{ \AA}$ dimension. The snapshots taken after (b) 0.1 , (c) 0.5 , and (d) 2.0 ns of equilibration are shown. The WCA values during the last 0.2 ns (gray background) were averaged and used as an equilibrium value.

were concentric around the center of mass of the droplet; for each bin, the inner boundary was displaced by 0.5 \AA along the horizontal axis until 20 bins with zero density were reached. To find the droplet boundary, each layer was fitted to the function

$$\rho(x) = a \cdot \left[1 - \tanh\left(\frac{x - x_0}{b}\right) \right] \quad (11)$$

which represents the decrease of the radial density. Here $\rho(x)$ is the radial density, a and b are proportional to the bulk liquid density and the thickness of the interface, respectively, and x_0 is the layer boundary. The layer boundary x_0 resulting from matching eq 11 to the radial density was fitted to a circular segment, the boundary within 5 \AA from the bottom being excluded. Fittings and contour plots were done using the fit command and cubic interpolation provided by MatLab v. 6.⁵⁸ The WCA was averaged over the last 0.2 ns for each MD simulation (see Figure 6). A few water molecules eventually evaporated from the droplet; water molecules 7 \AA away from the droplet were not taken into account.

3. Results and Discussion

In the following we report and discuss the results of our simulations. First, we describe the surface topography and how it is affected by the force fields and annealing cycles used. Second, we discuss the choice of system size and describe how the intermolecular parameters affect wetting of silica surfaces. Third, we present the determination of force field parameters optimal for describing wetting of silica surfaces. Finally, we illustrate the application of the new surface topography method and force field to the case of water permeation through silica nanopores.

3.1. Preparation of Annealed Surfaces. Table 1 summarizes the annealed surfaces obtained and their respective concentration of *DOs*, *DSis*, and *DAs*. Higher temperature and longer annealing using the GLASSFF_2.01 force field reduce the number of *DAs*, but not to the extent sufficient to obtain a silica surface with no *DAs*.

To obtain a silica surface with very few *DAs*, i.e., a minimum *DA* concentration, we employed the force field GLASSFF_1.01. Bakaev et al. were able to obtain hydrophobic silica surfaces with few *DAs* using nonlinear annealing schemes.^{51,63} In his original study, Bakaev employed an ionic pair potential (eq 2) with an additional dispersive term.³⁴ Due to the directionality added by the three-body potential in GLASSFF_2.01, *DAs* at the surface can easily be trapped into local minima corresponding to the tetrahedral configuration. The advantage of GLASSFF_1.01 is that it takes only two-body interactions into account and allows enough distortion of the tetrahedral arrangement to obtain a surface of silica without *DA*.

The maximum *DA* concentration for an amorphous planar surface is 4.6 nm⁻².²⁸ However, our annealing procedure did not result in a surface with a *DA* concentration higher than 2.9 nm⁻². A single minimization with either the GLASSFF_1.01 or the GLASSFF_2.01 force field decreases the *DA* concentration to 1.1 or 2.7 nm⁻², respectively. Even annealing at low temperatures and fixing 75% of the slab (cf. Table 1, SURF_3d4 and SURF_3d5) did not result in a higher *DA* concentration. We note that a *DA* concentration of 2.9 nm⁻² is close to the highest concentration of silanols (2.7 nm⁻²) for silica surfaces produced under a high vacuum,⁶⁹ where the silanol formation is reduced due to the anhydrous conditions. It would be interesting to investigate if a higher *DA* concentration can be obtained using a more advanced oxide glass force field.⁷⁰

The annealed surfaces introduced in subsection 2.2 (cf. Table 1) provided *DA* concentration in a range between 0.092 and 2.832 nm⁻² and were employed to simulate water–silica systems. The annealed surfaces modified into types I–IV (see subsection 2.2) were also employed this way. First, water disks were placed on top of the silica surfaces. Then, the resulting systems were employed to parametrize the intermolecular interactions using a CHARMM compatible silica force field. The results of our simulations are described in the next sections.

3.2. Influence of Droplet Size on Water Contact Angle. In using the WCA as a selection criterion of force field parameters, the question arises if simulated WCAs may depend on the size of droplets considered such that results may be biased. To determine the effect of the nanometer size of the water droplet on the WCA, we followed a procedure employed by Werder et al.²⁶ which is briefly described below. For a macroscopic droplet, the contact angle at equilibrium with an inert solid surface is determined by Young's equation, i.e., by

$$\gamma_{SV} = \gamma_{SL} + \gamma_{LV} \cos \theta_{\infty} \quad (12)$$

where θ_{∞} is the macroscopic WCA and γ_{LV} , γ_{SV} , γ_{SL} are the surface tensions at the liquid–vapor, solid–vapor, solid–liquid interfaces, respectively. To describe a microscopic droplet, a free energy correction to eq 12 needs to be taken into account. Macroscopic and microscopic contact angles can be correlated to each other using a modification of Young's equation⁷¹

$$\gamma_{SV} = \gamma_{SL} + \gamma_{LV} \cos \theta + \frac{\tau}{r_B} \quad (13)$$

$$\cos \theta = \cos \theta_{\infty} - \frac{\tau}{\gamma_{LV} r_B} \quad (14)$$

where θ is the microscopic WCA, τ is the line tension, and r_B is the radius of the base of the droplet.

Using eq 14, the variation of the WCA with droplet size can be determined by plotting $\cos \theta$ as a function of $1/r_B$. The plot has a slope proportional to τ , the sign of τ indicating if the WCA either increases or decreases with decreasing droplet size. Experimentally, the sign of τ is difficult to determine; its magnitude has been estimated to lie between 1×10^{-12} and 1×10^{-10} J m⁻¹,⁷² which is at the limit of experimental resolution. MD simulations using argon droplets on ideal smooth surfaces have shown that τ can be positive, negative, or even close to zero, depending on the magnitude of the intermolecular interactions between liquid and solid.⁷³

To calculate the slope τ/γ_{LV} in eq 14, we used the surface SURF_2b (cf. Table 1) with the lowest solvent accessible area and a minimum effect of surface roughness. In addition to our system of 1981 water molecules, two further systems were built: a smaller one with a water disk of height and radius of 22 Å (1039 water molecules) and a larger one with a water disk of height and radius of 35 Å (4059 water molecules). In the latter system, the annealed surface was replicated 4×4 times in the *X*- and *Y*-directions, and the periodicity was set to 229.2 Å \times 229.2 Å \times 229.2 Å; the systems were simulated for 2 ns and 5 ns, respectively, under the conditions described in Table 2. The slope τ/γ_{LV} showed no clear correlation with droplet size, suggesting either negligible or small negative values, probably due to the influence of surface roughness.⁷⁴ We decided then to parametrize our force field using a droplet consisting of 1981 water molecules and assuming the WCA to be independent of droplet size. A more detailed investigation of the relationship between WCA and surface roughness using different droplet sizes is beyond the scope of this study.

3.3. Dangling Atoms Enhance Electrostatic Silica–Water Interactions. After the annealed surfaces were obtained and the size of the water–silica system was specified, we proceeded to investigate how the force field parameters affect the wettability of different silica surfaces. Figure 6 shows the time dependence during a 2 ns MD simulation of the WCA for a droplet of 1981 water molecules resting on an annealed silica surface. A similar time dependence was seen for all annealed surfaces, showing an initial decrease within the first 1 ns, followed by an equilibrium state over the next 1 ns. Some of the systems were simulated for 4 ns, confirming that the systems reached equilibrium within the first 2 ns.

Figure 7 shows the dependence of the WCA on the silica intermolecular parameters for three silica surfaces: two annealed surfaces with *DA* concentrations of 0.092 and 2.093 nm⁻² and a surface corresponding to a “raw cut” of bulk amorphous silica without any minimization or annealing applied, with a *DA* concentration of 5.817 nm⁻². The parameter for the silicon well-depth (ϵ_{Si}) was varied from 0.06 to 0.4 kcal/mol while the

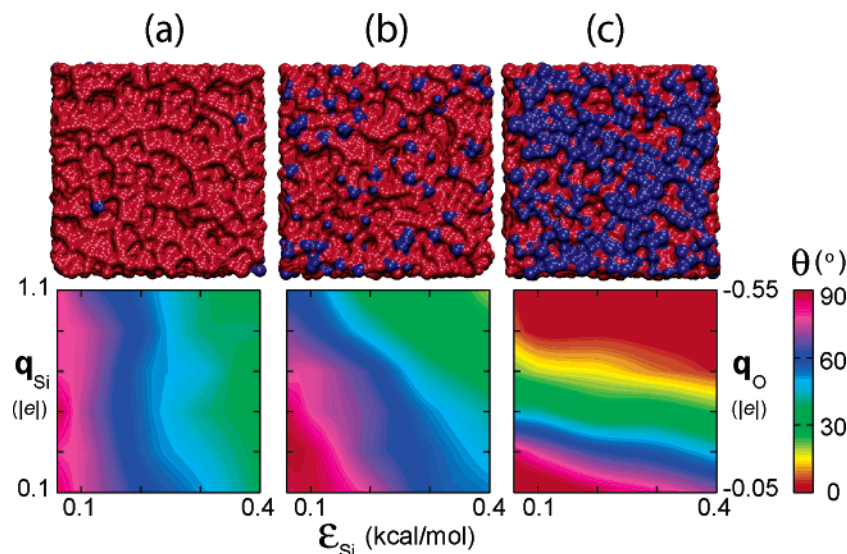


Figure 7. Concentration of dangling atoms (DA) affects the wetting properties of silica. The first row shows a top view of three silica slabs: two annealed surfaces (cf. Figure 3a) with a DA concentration of 0.09 nm^{-2} (a) and 2.09 nm^{-2} (b) and a “raw cut” surface with 5.82 nm^{-2} (c) (Table 1, surfaces SURF_2b, SURF_3b2, and SURF_Raw, respectively). Dangling atoms (DO and DSi) are colored in blue, and nondangling atoms are colored in red. The three contour plots in the second row illustrate the dependence of the WCA on silica intermolecular parameters. The value of the WCA is color-coded according to the colorbar at the right. The abscissa represents the variation of the vdW parameters for silica. The parameter for the silicon well-depth (ϵ_{Si}) varies from 0.06 to 0.4 kcal/mol. The ordinate represents the charge of the silicon atoms. The oxygen and silicon charges are changed simultaneously, keeping their ratio at $-1:2$. The charge of the oxygen atoms (q_{O}) varies from $-0.05 |e|$ to $-0.55 |e|$, while the charge of the silicon atoms (q_{Si}) varies from $0.1 |e|$ to $1.1 |e|$ (cf. Section 2). Clearly, the increase of the DA concentration enhances the electrostatic interactions between water and silica. For the surface with 0.09 nm^{-2} , the WCA value depends on ϵ_{Si} but is found rather independent of the charges q_{Si} and q_{O} . For the surface with 2.09 nm^{-2} , the WCA is determined by both ϵ_{Si} and q_{Si} (or q_{O}). In the case of (c), the WCA depends strongly on the magnitude of the partial charges.

oxygen and silicon charges were changed simultaneously, keeping their ratio constant, namely at a value of $-1:2$ (cf. Section 2). The WCA determined for the surface with the lowest DA concentration (Figure 7a) is seen to depend only on the magnitude of the vdW interaction and is insensitive to the partial charges of silicon and oxygen atoms. For a nonzero DA concentration, the partial charges can influence the WCA. Figure 7b shows a surface with a DA concentration of 2.093 nm^{-2} ; in this case, the WCA indeed is seen to depend to the same extent on vdW and electrostatic interactions, an increment in the magnitude of either of these interactions reducing the WCA. Figure 7c shows a surface with the highest DA concentration, corresponding to a “raw cut” of bulk amorphous silica; in this case the effect of the electrostatic interactions dominates.

The results described are consistent with previous MD studies^{51,52} which showed that DAs at the surface, like DOs and DSis, act as hydrophilic centers. The low affinity of bicoordinated oxygens (non-DAs) toward water has also been confirmed by experiment.⁷⁵ Fully coordinated atoms are partially buried at the surface; hence, their electrostatic contribution is effectively screened by their neighbors. Conversely, DAs are more exposed and the charges of q_{O} and q_{Si} produce oriented dipoles that act as adsorption sites for water.

3.4. Parametrization of Intermolecular Interactions. The main goal of the present study is to optimize force field parameters for the interactions of silica and water. For this purpose, the WCA was chosen as a selection criterion for optimization. Annealed surfaces were used as starting points to model the wetting properties of silica.

The first step in judging modeled wetting properties of silica is to establish the experimental observable that will serve as the criterion for optimality, namely the observed WCA. In the case of amorphous silica, the observed WCA can assume a range of values, depending on the concentration of silanol groups at the silica surface. Lamb et al.⁷⁷ have established a heuristic

relationship between WCA θ and the area fraction, a_{SiOH} , of silanols in polished silica plates:

$$\cos \theta = 0.257 a_{\text{SiOH}} + 0.743 \quad (15)$$

Here a_{SiOH} is the number of silanols per nm^2 divided by 4.6 nm^{-2} (the latter being the maximum silanol surface density).²⁸ From eq 15, a completely dehydroxylated silica surface without any silanols ($a_{\text{SiOH}} = 0$) would exhibit a WCA of 42° , whereas a fully hydroxylated surface ($a_{\text{SiOH}} = 1$) is completely hydrophilic and has a WCA of zero. In the following we will employ eq 15 as a reference for experimentally observed WCAs for silica surfaces with different silanol concentrations. Comparison of the results of eq 15 with the results from simulations will permit us to select optimal force field parameters.

For the annealed surfaces defined in section 2.2, we have varied the force field parameters to find the values that reproduce the WCA. In the case of these surfaces, two parameters are unknown and, hence, can be varied: ϵ_{Si} and one of the partial atomic charges, either q_{Si} or q_{O} (cf. subsection 2.3 and Table 2). We started by considering first a surface with very few DAs and, hence, $a_{\text{SiOH}} = 0$ (surface SURF_2b in Table 1). Figure 7a shows such a surface (that is similar to a completely dehydroxylated silica surface) and the ϵ_{Si} - and q_{Si} -dependence of the associated WCA. As can be seen, the WCA is independent of q_{Si} (or q_{O}) and depends only on ϵ_{Si} ; therefore, we obtained the optimal value for one of the two parameters, namely ϵ_{Si} . In fact, an ϵ_{Si} value of 0.3 kcal/mol reproduces a WCA of about 42° suggested by eq 15.

The next step is to parametrize the partial atomic charges q_{Si} and q_{O} . Figure 7b and 7c show that, as the DA concentration increases, the effect of q_{Si} and q_{O} on wetting also increases. Therefore, a straightforward strategy consisted of choosing a range of surfaces with different DA concentrations and using them to find parameters for the partial atomic charges that match

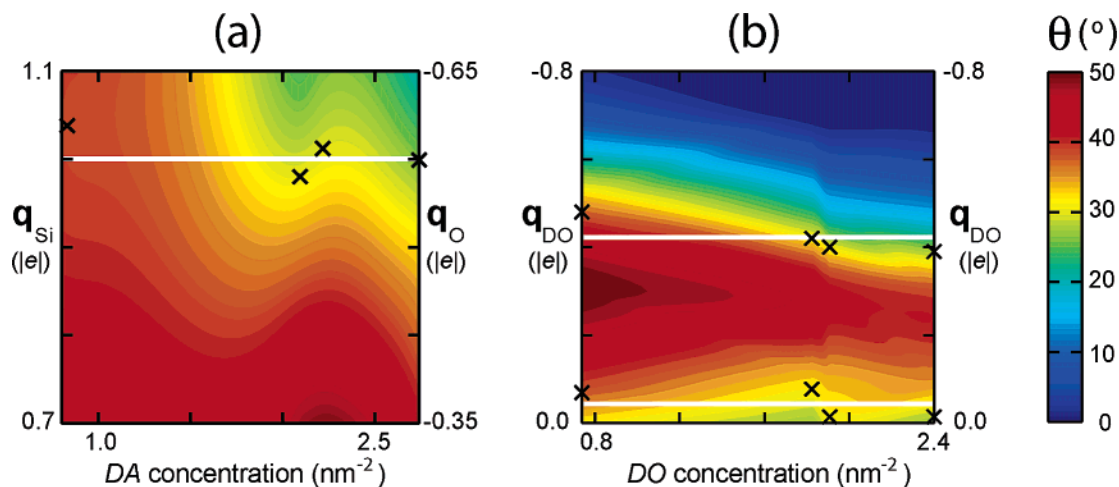


Figure 8. Dependence of the WCA on the concentration of surface defects (cf. Figure 3a and 3b). The contour plot shows the value of the WCA (color coded), and the X-axis shows the concentration of surface defects, either DA (a) or DO (b). The Y-axis shows the variation of the electrostatic parameters. The black crosses indicate the experimental WCAs for different silanol concentrations based on eq 15. (a) Four annealed surfaces with concentrations 0.831 nm^{-2} , 2.093 nm^{-2} , 2.216 nm^{-2} , and 2.739 nm^{-2} were simulated (Table 1, surfaces SURF_2b, SURF_3b1, SURF_3b2, and SURF_3b3, respectively). The wettability of silica can be reproduced using a single set of charges, $1.0 |e|$ for silicon and $-0.5 |e|$ for oxygen (white line). (b) Four surfaces of type I with concentrations of DO of 0.739 nm^{-2} , 1.824 nm^{-2} , 1.908 nm^{-2} , and 2.400 nm^{-2} were simulated. Two values of q_{DO} can reproduce the experimental wetting curve: $q_{\text{DO}} = -0.044 |e|$ and $q_{\text{DO}} = -0.423 |e|$. Table 4 summarizes the parameters that reproduce silica wetting for annealed surfaces and surfaces of type I.

eq 15. We used for this purpose the surfaces with DA concentrations of 0.831 nm^{-2} , 2.093 nm^{-2} , 2.216 nm^{-2} , and 2.739 nm^{-2} , permitting us to calibrate the charges q_{O} and q_{Si} with all vdW parameters fixed (cf. section 2).

Figure 8a depicts the dependence of the WCA (color-coded) on the DA concentration (X-axis) and silica charges (Y-axis). We assumed that DAs control the adsorption properties of silanols. Even though those surfaces did not have explicit silanols, exposed DOs and DSis mimic the behavior of silanols in the sense that they act as adsorption centers of diverse intensity⁷⁶ with different affinities toward water.^{51,52} In amorphous silica, silanols also have different adsorption properties due to the heterogeneity of the silica surface. Our results show that an increment in either the charges or the DA concentration decreases the WCA. One can recognize from Figure 8a that point charges $q_{\text{Si}} = 1.0 |e|$ and $q_{\text{O}} = -0.5 |e|$ (white line) reproduce closely the experimentally observed WCAs as described by eq 15.

The method we employed for determining partial atomic charge deviates from the standard ab initio methods. Ab initio procedures estimate the point charges by fitting the electrostatic potential of small model fragments. However, amorphous materials are fairly heterogeneous. Clearly, one will have to define several types of O and Si atoms based on their local environment, the bonding structure, or both. Our approach provides a straightforward method for calculating a single set of charges that reproduce the surface hydrophobicity.

For surfaces of type I (cf. Figure 3b) we had to match the WCA by varying only q_{DO} , the charge of DOs, that was assumed to be different from the charge of oxygen in the bulk. Figure 8b presents the relevant results. The parameters assumed for the bulk atoms are given in Table 2. The WCA shows a clear dependence on the DO concentration. However, the effect of q_{DO} is not straightforward. As q_{DO} becomes more negative, the WCA shows an initial increase; at a q_{DO} value around $-0.3 |e|$, there is a change in behavior and the WCA starts to decrease continuously. One can recognize from Figure 8b that the experimental wettability described by eq 15 can be reproduced for two values of q_{DO} , namely $-0.044 |e|$ and $-0.423 |e|$.

We suggest that the initial increase in the hydrophobicity of surfaces of type I with decreasing q_{DO} is due to the oriented dipole moment of the exposed SiO_4 tetrahedras which contain DOs. For a perfect SiO_4 tetrahedron with a vanishing dipole moment, each oxygen atom contributes a charge of $-q_{\text{Si}}/4$. In the case of surfaces of type I, we assigned a charge of $q_{\text{Si}} = 0.9 |e|$. Assuming a tetrahedron with perfect symmetry, a value of $q_{\text{DO}} = -0.225 |e|$ cancels out the dipole moment. Any value of q_{DO} different from $-0.225 |e|$ produces a nonvanishing dipole moment; for $q_{\text{DO}} < -0.225 |e|$ the direction of the dipole is to the exterior of the surface, and for $q_{\text{DO}} > -0.225 |e|$ it is to the interior. In Figure 8b, the change in the wetting behavior occurs around $q_{\text{DO}} = -0.3 |e|$. The difference to the estimated value of $-0.225 |e|$ should be due to distortions of the tetrahedron as well as due to the amorphous topography. Indeed, the wetting properties of a surface are strongly dependent on the dipole moment at the solid surface.^{78,79} Bakaev et al.⁵¹ have shown that dipoles originating from surface defects, such as DOs, produce strong hydrophobic sites. Thus, it is likely that the switch in the wetting behavior observed around $q_{\text{DO}} = -0.3 |e|$ is due to a change in the dipole moment.

Up to this point, the WCA was found to be reproducible for nonhydroxylated surfaces: the annealed surfaces and surfaces of type I. The next logical step was to consider silica surfaces of type II, III, and IV (cf. Figure 3c–e), which have hydroxyl groups and offer an opportunity to parametrize the silanol groups. For all parameter combinations tested (cf. Table 3), the silanol group acted as a strong hydrophilic center and produced a WCA value of 0° . Complete wetting ($\theta = 0$) was observed even for a silanol concentration as small as 1 nm^{-2} , which proves that the heterogeneity of the surface was lost. Figure 9 illustrates wetting for one of those cases, a surface of type IV decorated with deprotonated vicinal silanols, with $q_{\text{total}} = 0$ (cf. subsection 2.3 and Figure 4). We conclude that reproducing correct WCAs readily yields parameters characterizing the surface hydrophobicity, but the approach is not suitable to parametrize uniquely the silanol group; instead a broad range of silanol group parameters yields the same hydrophilic surface property.

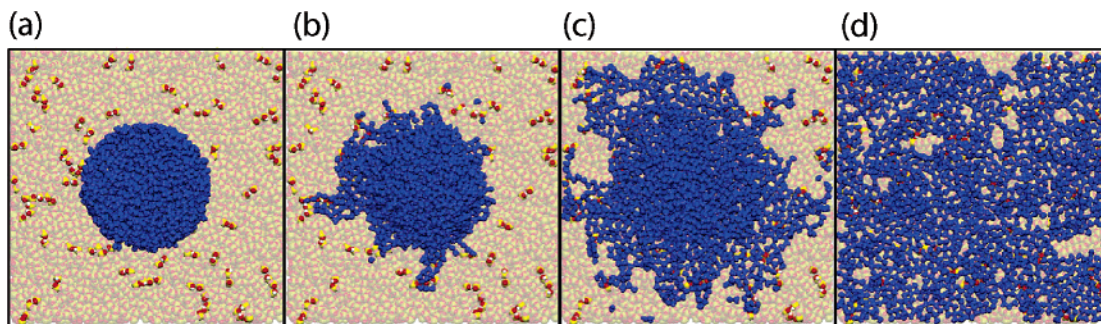


Figure 9. Silanol groups enhance surface hydrophilicity. Surface silanols (pictured as opaque yellow, red, and white points) produce complete wetting, independent of the charge parameters. Snapshots correspond to (a) 0, (b) 0.12, (c) 0.64, and (d) 2.0 ns of a MD simulation of a water disk (blue) resting on top of the silica surface with a silanol concentration of 1.0 nm^{-2} . (b) and (c) show that initial spreading of the water molecules over the surface is being guided by the locations of surface silanols. (d) shows complete wetting of the silica surface.

TABLE 4: Intermolecular Parameters that Reproduce Silica Wetting for Annealed and Type I Surfaces

surface	ϵ_{Si} (kcal/mol)	ϵ_{O} (kcal/mol)	$r_{\text{Si}}^{\text{min}}$ (Å)	$r_{\text{O}}^{\text{min}}$ (Å)	q_{Si} (e)	q_{O} (e)	q_{DO} (e)
annealed	0.3	0.15	3.5	4.295	1.0	−0.50	
type I (1st solution)	0.3	0.15	3.5	4.295	0.9	−0.45	−0.044
type I (2nd solution)	0.3	0.15	3.5	4.295	0.9	−0.45	−0.423

Judging by agreement of the measured WCAs with eq 15, the best surface models are given in Table 4. The wetting properties of silica can be reproduced using annealed surfaces and surfaces of type I. In the latter case, two sets of parameters reproduce wetting, likely due to a change on the surface dipole when changing the charge q_{DO} . Parametrization of silanol groups requires a different approach which should take into account the different types of silanols and their protonation states.

3.5. Water Permeation through Silica Pores. The simulation results reported above allowed us to calibrate a CHARMM-like force field that properly describes the wettability of silica surfaces. With this force field (Table 4), one is able to simulate now silica–water systems as they arise in silica nanopores.

The silica pores were annealed following the cycles described in Table 1. Similar to silica slabs, the annealing cycle with the GLASSFF_1.01 force field produced a pore with the lowest solvent accessible surface area and the lowest *DA* concentration. Annealing cycles with the GLASSFF_2.01 force field produced pores with higher *DA* concentrations; however, no straightforward relationship could be established between solvent accessible surface area and *DA* concentration (cf. Table 1). During all annealing procedures, the diameter of the pore shrank by less than 2 Å relative to its initial value of 20 Å.

We simulated the permeation of water through the annealed pores using the intermolecular parameters validated by our simulations (Table 4). The pores were covered with a water box on each side, and the resulting systems were equilibrated for 1 ns at 300 K under different conditions (see below). The number of water molecules within the pore was used as a measure of permeation. To count the number of water molecules in the pore, we considered a cylindrical bin of 32 Å diameter concentric with the pore axis, with a height of 44 Å parallel to the *Z*-axis.

Figure 10a–c present the time dependence of the number of water molecules in the pores simulated in the *NpT* ensemble with applied pressures of 1, 0.1, and 0.01 atm, respectively. The pore with the highest *DA* concentration (PORE_Raw) showed the fastest permeation in all cases (black lines). For all other pores, permeation was slower and pressure differences did not speed up permeation.

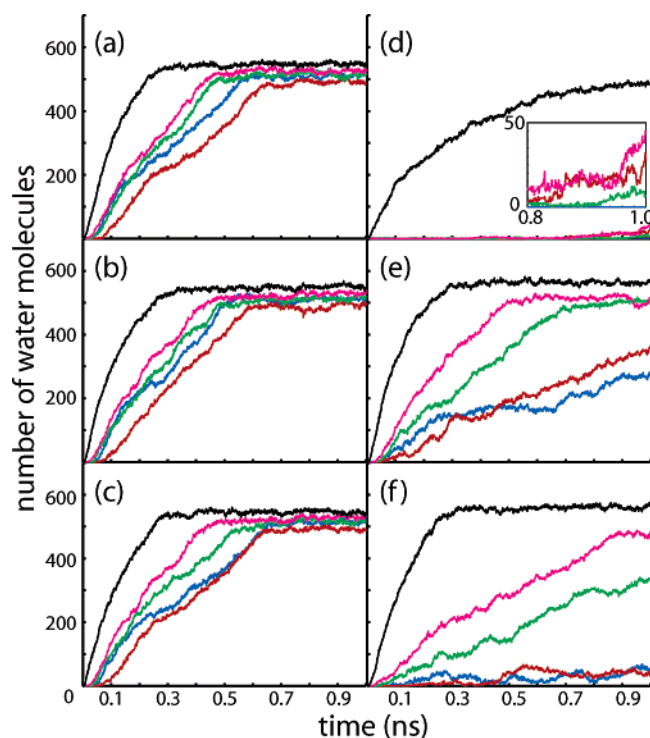


Figure 10. Water permeation of silica pores during 1 ns MD simulations. Each color corresponds to a pore with a different concentration of *DAs*: 0.027 nm^{-2} (blue), 0.601 nm^{-2} (red), 1.618 nm^{-2} (green), 2.042 nm^{-2} (purple), and 4.244 nm^{-2} (black) (Table 1, pores PORE_2b, PORE_3b1, PORE_3b2, PORE_Min and PORE_Raw, respectively). (a–c) Traces from *NpT* ensemble simulations using silica parameters from Table 4 and a pressure of (a) 1 atm, (b) 0.1 atm, (c) 0.01 atm. (d) Traces from *NVT* ensemble simulations at zero pressure. (e, f) Traces of *NpT* ensemble simulations at 1 atm pressure using silica parameters from Table 4, except for ϵ_{Si} that was set to (e) 0.1 kcal/mol and (f) 0.01 kcal/mol.

Figure 10d shows the permeation simulated assuming an *NVT* ensemble. Under this condition, PORE_Raw is the only pore filled with water after 1 ns. The inset in Figure 10d shows the last 0.2 ns of the simulations. The pore with very few *DAs* (PORE_2b, blue line) does not allow a single water molecule into the pore, revealing the importance of *DA* concentration for water permeation.

In the case of inorganic solid nanopores, such as Si_3N_4 and SiO_2 , wetting a dry pore in the laboratory could take from 20 to 60 h.¹⁴ It has been proposed that electron beams used to drill the pores locally melt the silica.^{13,80} We note that UV laser beams are also known to dehydroxylate silica surfaces.⁸¹ Thus, it might be possible that the initial nanopore hydrophobicity is due to electron beam drilling that leads to the formation of a hydrophobic surface, like the one of pore PORE_2b. The corresponding behavior is observed in our *NVT* ensemble simulations.

We tested if the internal pressure due to air molecules in the pore could be responsible for the initial nonwetting behavior of the nanopore. The ideal gas law predicts about one gas molecule on average for a volume of 41 nm³ at 300 K and 1 atm, i.e., less than one gas molecule in our nanometer-radius pores. But, according to Laplace's equation, the pressure inside a curved surface (P_{in}), like a bubble trapped inside the nanopore, is always higher than the pressure outside (P_{ex}). The relationship is

$$P_{\text{in}} = P_{\text{ex}} + \frac{2\gamma}{r} \quad (16)$$

where γ is the surface tension of water and r is the radius of the bubble. Considering a bubble of around 5 nm radius and a γ value of 72.8 dyn/nm², the internal pressure would be around 30 atm. If we assume the ideal gas law, 18 gas molecules are inside the nanopore; if we assume the vdW equation for gases instead, only 2 or 3 gas molecules are inside.

The question arises if gas molecules trapped inside the nanopore can prevent pore hydration. We attempted to answer this question through simulations. For this purpose, we prepared an equilibrated system with an empty cylinder of 35 Å height inside the pore starting from a snapshot of an earlier simulation with PORE_2b under *NpT* conditions at 1 atm. We produced a less hydrophobic surface in the pore by decreasing ϵ_{Si} to 0.2 kcal/mol from its original value of 0.3 kcal/mol, to slow the permeation seen in Figure 10a and observe in detail the dynamics of the air molecules. To represent air, we used 15 inert beads with a well depth ϵ_{gas} of 2.0×10^{-5} kcal/mol and radius $r_{\text{gas}}^{\text{min}}$ of 8 Å. The values adopted emulate a hydrophobic bead with low solubility.

All gas beads were located at the center of the pore and were not interacting with each other but interacted with water; the lack of mutual interaction mimics ideal gas behavior. The simulations were carried out using the local enhancement sampling protocol.⁸² In the simulations we control the temperature and, thereby, the pressure of the gas by coupling the gas beads to a Langevin bath that was independent from the remainder of the system. Three temperatures were assumed for the gas beads: 300, 3000, and 6000 K (these temperatures correspond to pressures of 25, 250, and 500 atm, according to the ideal gas law). The three systems were simulated for 0.7, 0.9, and 0.9 ns, respectively. In the first two cases, water completely permeated the nanopore; in the last case, water did not penetrate the pore completely by the end of the 0.9 ns but compressed the gas to a small cylindrical volume of 12 Å height. We conclude that air molecules trapped inside the nanopore cannot be responsible for the initial low water permeability of the pores; rather the surface hydrophobicity slows down the wetting (cf. Figure 10d). However, we cannot rule out the possibility that in real systems larger air bubbles are trapped in the supporting structure (i.e., below and above the pore).

To further test the effect of the surface hydrophobicity on wetting, we increased the hydrophobicity of the silica nanopore and analyzed the permeation kinetics. Figure 10e and 10f show water permeation simulated in the *NpT* ensemble under 1 atm, when the value of ϵ_{Si} was changed to 0.1 and 0.01 kcal/mol, respectively. In either case, we observe that ϵ_{Si} affects the permeation speed. Furthermore, the velocity of the permeation is faster for pores with a higher concentration of DAs. In these two cases, the permeation behavior can be explained in terms of cohesive (water–water) and adhesive (water–silica) forces. ϵ_{Si} controls the magnitude of the adhesive forces and, hence, determines the permeation kinetics.

4. Conclusion

We have developed a force field for amorphous silica surfaces that reproduces experimental wetting properties of silica surfaces with different concentrations of silanols based on the observable WCA. The route that we followed is different from conventional parametrization schemes and, to our knowledge, has not been used in a similar manner before.

Our main results are summarized in Table 4. We find that atomic level details of the silica surface, such as dangling atoms (DAs), need to be taken into account when one seeks to describe accurately silica–water interactions. Our simulations have shown that annealed silica surfaces with DAs capture the heterogeneity of realistic surfaces and are good representations of the silica structures. We conclude, therefore, that the surface reconstruction through annealing cycles is a necessary step for simulating amorphous silica–water systems. For building hydrophobic silicas, annealings with two-body potentials are recommended over the three-body ones, as they permit larger distortions of the surface geometry.

Our atomic-level silica model is appropriate for MD simulations of confined environments such as nanopores, where the silica topography is an important factor. The results explain the initial hydrophobicity of manufactured silica nanopores. The model is currently being employed to simulate ion conduction through silica nanopores and binding affinities of various biological macromolecules to silica surfaces.

Acknowledgment. We thank Jerome Baudry for assistance in performing simulations with the Cerius² program using the clusters of the School of Chemical Sciences at UIUC and Gregory Timp for valuable insights into silicon nanopores. We also thank the members of the Theoretical and Computational Biophysics Group for helpful discussions. This work is supported by grants from the NIH (P41-RR05969, R01-HG003713A) and DARPA (392-FA95501). We acknowledge supercomputer time provided at the National Center for Supercomputing Applications through National Resources Allocation Committee Grant MCA93S028 and MCA05S028.

References and Notes

- (1) Mull, D.; Sorsch, T.; Moccio, S.; Baumann, F.; Evas-Lutterodt, K.; Timp, G. *Nature (London)* **1999**, 399, 758–761.
- (2) Nawrocki, J. *J. Chromatogr. A* **1997**, 779, 29–71.
- (3) Yoo, K. H.; Ha, D. H.; Lee, J. O.; Park, J. W.; Kim, J.; Kim, J. J.; Lee, H. Y.; Kawai, T.; Choi, H. Y. *Phys. Rev. Lett.* **2001**, 87, 198102–1–198102–4.
- (4) Mirkin, C. A.; Taton, A. T. *Nature (London)* **2000**, 405, 626–627.
- (5) Yeung, E. S. *Annu. Rev. Phys. Chem.* **2004**, 55, 97–126.
- (6) Heller, M. J. *Annu. Rev. Biomed. Eng.* **2002**, 4, 129–153.
- (7) Kang, S. H.; Shortreed, M. R.; Yeung, E. S. *Anal. Chem.* **2001**, 73, 1091–1099.
- (8) Tarasevich, Y. I.; Monakhova, L. I. *Colloid J.* **2002**, 64, 482–487.

- (9) Romanowski, G.; Lorenz, M. G.; Wackernagel, W. *Appl. Environ. Microbiol.* **1991**, *57*, 1057–1061.
- (10) Balladur, V.; Theretz, A.; Mandrand, B. *J. Colloid Interface Sci.* **1997**, *194*, 408–418.
- (11) Gray, J. J. *Curr. Opin. Struct. Biol.* **2004**, *14*, 110–115.
- (12) Braun, R.; Sarikaya, M.; Schulten, K. *J. Biomater. Sci., Polym. Ed.* **2002**, *13*, 747–758.
- (13) Storm, A. J.; Chen, J. H.; Ling, X. S.; Zandbergen, H. W.; Dekker, C. *Nat. Mater.* **2003**, *2*, 537–540.
- (14) Ho, C.; Qiao, R.; Heng, J. B.; Chatterjee, A.; Timp, R. J.; Aluru, N. R.; Timp, G. *Proc. Natl. Acad. Sci. U.S.A.* **2005**, *102*, 10445–10450.
- (15) Austin, R. *Nat. Mater.* **2003**, *2*, 567–568.
- (16) Heng, J. B.; Aksimentiev, A.; Ho, C.; Dimitrov, V.; Sorsch, T.; Miner, J.; Mansfield, W.; Schulten, K.; Timp, G. *Bell Labs Technol. J.* **2005**, *10*, 5–22.
- (17) Slater, G. W.; Desruisieux, C.; Hubert, S. J.; Mercier, J.; Labrie, J.; Boileau, J.; Tessier, F.; Pépin, M. P. *Electrophoresis* **2000**, *21*, 3873–3887.
- (18) Service, R. F. *Science* **2006**, *311*, 1544–1546.
- (19) Church, G. *Mol. Syst. Biol.* **2005**, *1*, 100040-E1–100040-E3.
- (20) Heng, J. B.; Aksimentiev, A.; Ho, C.; Marks, P.; Grinkova, Y. V.; Sligar, S.; Schulten, K.; Timp, G. *Nano Lett.* **2005**, *5*, 1883–1888.
- (21) Aksimentiev, A.; Heng, J. B.; Timp, G.; Schulten, K. *Biophys. J.* **2004**, *87*, 2086–2097.
- (22) Heng, J. B.; Ho, C.; Kim, T.; Timp, R.; Aksimentiev, A.; Grinkova, Y. V.; Sligar, S.; Schulten, K.; Timp, G. *Biophys. J.* **2004**, *87*, 2905–2911.
- (23) Gracheva, M. E.; Xiong, A.; Leburton, J.-P.; Aksimentiev, A.; Schulten, K.; Timp, G. *Nanotechnology* **2006**, *17*, 622–633.
- (24) Gracheva, M. E.; Aksimentiev, A.; Leburton, J.-P. *Nanotechnology* **2006**, *17*, 3160–3165.
- (25) Harding, J. H.; Duffy, D. M. *J. Mater. Chem.* **2006**, *16*, 1105–1112.
- (26) Werder, T.; Walther, J. H.; Jaffe, R. L.; Halicioglu, T.; Koumoutsakos, P. *J. Phys. Chem. B* **2003**, *107*, 1345–1352.
- (27) Iler, R. *The chemistry of silica*; John Wiley and Sons: New York, Chichester, Brisbane, Toronto, 1979.
- (28) Zhuravlev, L. T. *Colloids Surf., A* **2000**, *173*, 1–38.
- (29) Curthoys, G.; Davydov, V. Y.; Kiselev, A. K.; Kiselev, S. A.; Kuznetsov, B. V. *J. Colloid Interface Sci.* **1974**, *48*, 58–72.
- (30) Palit, D.; Moulik, S. P. *J. Colloid Interface Sci.* **2001**, *239*, 20–26.
- (31) Ong, S.; Zhao, X.; Eisenthal, K. *Chem. Phys. Lett.* **1992**, *191*, 327–335.
- (32) Bolt, G. H. *J. Phys. Chem.* **1957**, *61*, 1166–1169.
- (33) Behrens, S. H.; Grier, D. G. *J. Chem. Phys.* **2001**, *115*, 6716–6721.
- (34) Tsuneyuki, S.; Tsukada, M.; Aoki, H. *Phys. Rev. Lett.* **1988**, *61*, 869–872.
- (35) Hill, J. R.; Sauer, J. *J. Phys. Chem.* **1994**, *98*, 1238–1244.
- (36) van Beest, B. W. H.; Kramer, G. J. *Phys. Rev. Lett.* **1990**, *64*, 1955–1958.
- (37) Feuston, B. P.; Garofalini, S. H. *J. Chem. Phys.* **1988**, *89*, 5818–5824.
- (38) Flikkema, E.; Bromley, S. T. *Chem. Phys. Lett.* **2003**, *378*, 622–629.
- (39) Jorgensen, W. L.; Chandrasekhar, J.; Madura, J. D.; Impey, R. W.; Klein, M. L. *J. Chem. Phys.* **1983**, *79*, 926–935.
- (40) Berweger, C. D.; van Gunsteren, W. F.; Müller-Plathe, F. *Chem. Phys. Lett.* **1995**, *232*, 429–436.
- (41) Gallo, P.; Ricci, A.; Rovere, M. *J. Chem. Phys.* **2002**, *116*, 342–346.
- (42) Gallo, P.; Rapinesi, M.; Rovere, M. *J. Chem. Phys.* **2002**, *117*, 369–375.
- (43) Rovere, M.; Ricci, M. A.; Vellati, D.; Bruni, F. *J. Chem. Phys.* **1998**, *108*, 9859–9867.
- (44) Guéan, R.; Morineau, D.; Alba-Simionesco, C. *Chem. Phys.* **2005**, *317*, 236–244.
- (45) Leung, K.; Rempe, S. B.; Lorenz, C. D. *Phys. Rev. Lett.* **2006**, *96*, 095504-1–095501-4.
- (46) Levine, S. M.; Garofalini, S. H. *J. Chem. Phys.* **1987**, *86*, 2997–3002.
- (47) Feuston, B. P.; Garofalini, S. H. *J. Chem. Phys.* **1989**, *91*, 564–570.
- (48) Garofalini, S. H. *J. Non-Cryst. Solids* **1990**, *120*, 1–12.
- (49) Feuston, B. P.; Garofalini, S. H. *J. Appl. Phys.* **1990**, *68*, 4830–4836.
- (50) Webb III, E. B.; Garofalini, S. H. *J. Non-Cryst. Solids* **1998**, *226*, 47–57.
- (51) Bakaev, V. A.; Steele, W. A. *J. Chem. Phys.* **1999**, *111*, 9803–9812.
- (52) Leed, E. A.; Pantano, C. G. *J. Non-Cryst. Solids* **2003**, *325*, 48–60.
- (53) Lopes, P. E. M.; Murashov, V.; Tazi, M.; Demchuk, E.; MacKerell, A. D., Jr. *J. Phys. Chem. B* **2006**, *110*, 2782–2792.
- (54) Foloppe, N.; MacKerell, A. D., Jr. *J. Comput. Chem.* **2000**, *21*, 86–104.
- (55) MacKerell, A. D., Jr.; Bashford, D.; Bellott, M.; Dunbrack, R. L., Jr.; Evanseck, J.; Field, M. J.; Fischer, S.; Gao, J.; Guo, H.; Ha, S.; Joseph, D.; Kuchnir, L.; Kuczera, K.; Lau, F. T. K.; Mattos, C.; Michnick, S.; Ngo, T.; Nguyen, D. T.; Prodhom, B.; Reiher, I. W. E.; Roux, B.; Schlenkrich, M.; Smith, J.; Stote, R.; Straub, J.; Watanabe, M.; Wiorkiewicz-Kuczera, J.; Yin, D.; Karplus, M. *J. Phys. Chem. B* **1998**, *102*, 3586–3616.
- (56) Cerius², v.4.9; Accelrys, Inc.: 2003.
- (57) Phillips, J. C.; Braun, R.; Wang, W.; Gumbart, J.; Tajkhorshid, E.; Villa, E.; Chipot, C.; Skeel, R. D.; Kale, L.; Schulten, K. *J. Comput. Chem.* **2005**, *26*, 1781–1802.
- (58) Matlab, v.6.; The MathWorks, Inc.: 2002.
- (59) Humphrey, W.; Dalke, A.; Schulten, K. *J. Mol. Graphics* **1996**, *14*, 33–38.
- (60) Zirl, D. M.; Garofalini, S. H. *J. Am. Ceram. Soc.* **1990**, *73*, 2848–2856.
- (61) Bondi, A. *J. Phys. Chem.* **1964**, *68*, 441–451.
- (62) Mayo, S. L.; Olafson, B. D.; Goddard, W. A., III. *J. Phys. Chem.* **1990**, *94*, 8897–8909.
- (63) Bakaev, V. A. *Phys. Rev. B* **1999**, *60*, 10723–10726.
- (64) Huff, N. T.; Demiralp, E.; Çagin, T.; Goddard, W. A., III. *J. Non-Cryst. Solids* **1999**, *253*, 133–142.
- (65) Grubmüller, H.; Heller, H.; Windemuth, A.; Schulten, K. *Mol. Simul.* **1991**, *6*, 121–142.
- (66) Schlick, T.; Skeel, R.; Brünger, A.; Kalé, L.; Board, J. A., Jr.; Hermans, J.; Schulten, K. *J. Comput. Phys.* **1999**, *151*, 9–48.
- (67) Martyna, G. J.; Tobias, D. J.; Klein, M. L. *J. Chem. Phys.* **1994**, *101*, 4177–4189.
- (68) de Ruijter, M. J.; Blake, T. D.; De Coninck, J. *Langmuir* **1999**, *15*, 7836–7847.
- (69) D'Souza, A. S.; Pantano, C. G. *J. Am. Ceram. Soc.* **1999**, *82*, 1289–1293.
- (70) Maranas, J. K.; Chen, Y. *J. Chem. Phys.* **2001**, *115*, 6578–6589.
- (71) Wang, J. Y.; Betelu, S.; Law, B. M. *Phys. Rev. E* **2001**, *63*, 031601-1–031601-11.
- (72) Drelich, J. *Colloids Surf., A* **1996**, *116*, 43–54.
- (73) Guo, H. K.; Fang, H. P. *Chin. Phys. Lett.* **2005**, *22*, 787–790.
- (74) Checchio, A.; Guenoun, P.; Dailant, J. *Phys. Rev. Lett.* **2003**, *91*, 186101-1–186101-4.
- (75) Yates, J. T., Jr. *Surf. Sci.* **2004**, *565*, 103–106.
- (76) Stallons, J. M.; Iglesia, E. *Chem. Eng. Sci.* **2001**, *56*, 4205–4216.
- (77) Lamb, R. N.; Furlong, D. N. *J. Chem. Soc., Faraday Trans. 1* **1982**, *78*, 61–73.
- (78) Graupe, M.; Takenaga, M.; Koini, T.; Colorado, R., Jr.; Lee, T. R. *J. Am. Chem. Soc.* **1999**, *121*, 3222–3223.
- (79) Krilov, G.; Laird, B. B. *Mol. Phys.* **2000**, *98*, 651–656.
- (80) Storm, A. J.; Chen, J. H.; Ling, X. S.; Zandbergen, H. W.; Dekker, C. *J. Appl. Phys.* **2005**, *98*, 014307-1–014307-8.
- (81) Halfpenny, D. R.; Kane, D. M.; Lamb, R. N.; Gong, B. *Appl. Phys. A* **2000**, *71*, 147–151.
- (82) Elber, R.; Karplus, M. *J. Am. Chem. Soc.* **1990**, *112*, 9161–9175.